A Design Methodology of Multiresonant Controllers for High Performance 400 Hz Ground Power Units

Felix Rojas , *Member, IEEE*, Roberto Cardenas , *Senior Member, IEEE*,
Jon Clare , *Senior Member, IEEE*, Matias Diaz , *Member, IEEE*, Javier Pereda , *Member, IEEE*,
and Ralph Kennel, *Senior Member, IEEE*

***Abstract*—In aerospace applications, a ground power unit has to provide balanced and sinusoidal 400 Hz phase-to-neutral voltages to unbalanced and nonlinear single-phase loads. Compensation of high-order harmonics is complex, as the ratio between the sampling frequency and compensated harmonics can be very small. Thus, multiple superimposed resonant controllers or proportional-integral (PI) nested controllers in multiple dq frames are not good alternatives. The first approach cannot ensure stability, while the second cannot track the sinusoidal zero-sequence components typically present in unbalanced systems, and unattainably high bandwidth at the inner current control loop is typically required. In this paper, a simple methodology for designing a single-loop, multiple resonant controller for simultaneous mitigation of several high-order harmonics, ensuring stability, is presented. Experimental results, based on a 6 kW four-leg neutral point clamped converter, validate the proposed controller design, showing excellent steady-state and transient performance.**

***Index Terms*—Four-leg converters, resonant controllers, three-level neutral point clamped (NPC) inverter.**

I. INTRODUCTION

RECENTLY, the aircraft industry has faced a tremendous development in the technology used for communication,

services, and control systems within an aircraft [1]. Electronic devices have played a fundamental role in this growth, leading to a more complex and sophisticated electrical system within the plane, which has to fulfill stringent power quality and safety regulations [2], [3]. When the aircraft is on ground, a power converter-based ground power unit (GPU) is connected to it, providing 110 V phase-to-neutral at 400 Hz [2].

The aircraft electrical system is a four-wire unbalanced system, with many individual loads connected phase-to-neutral. Therefore, a GPU is a four-wire power supply rated at 110 V (phase), 400 Hz, and typically between 30–180 kVA (90 kVA being the most utilized power rate) [4].

Different solutions have been proposed for power electronics-based GPUs [5]. Typically, three H-bridges connected in parallel, sharing the same dc-link and connected to *LC* filters, are used to independently control each phase-to-neutral voltage. However, the compensation of high-order harmonic components is limited by the switching frequency. An alternative configuration uses transformers to add the output voltages of several inverters, generating a stepped waveform [6]. Although this configuration offers good total harmonic distortion (THD) with low switching frequency, it is complex to control and the high number of elements reduces its reliability. Recently new topologies such as matrix converters have been proposed for GPU applications [7], [8]. Despite advantages in terms of size and weight, this approach has a high number of switches and, for unbalanced load operation, produces distorted currents with low power quality in the input side of the converter.

The relatively high output frequency of the GPU is an issue for design. Standard 50/60 Hz uninterruptible power supply (UPS) converters typically have sampling frequencies between 2–12 kHz. The high ratio between the fundamental and the sampling frequency allows many control schemes, such as nested *d-q* controllers, resonant controllers, repetitive and predictive controllers [9]–[11] to be implemented relatively easily. However, for a 400 Hz GPU, a 2 kHz sampling frequency is not feasible, because the ratio between the fundamental and the sampling frequency is insufficient. Therefore, for a GPU, the sampling frequency typically has to be around 10–15 kHz and even higher when harmonic compensation is required. Moreover, the high bandwidth required for an inner current control

loop means the use of double-loop structures for nested voltage/current controllers is not practically implementable and the use of single-loop voltage controllers have been preferred for this application. In [4], a robust single-loop strategy has been proposed to control the output voltage of a GPU and whilst it achieves good performance with linear loads, it is not capable of compensating harmonic distortion with nonlinear loads.

Due to their simple and robust implementation, resonant controllers are an interesting solution for high-order harmonic compensation. They have been used for selective harmonic elimination in several applications [5], [7], [12]. However, careful consideration of stability margins and the selection of the discretization method are important during the controller design to ensure stability, particularly when high-order harmonics have to be compensated [13]–[15]. In [5], a resonant controller has been proposed as a solution for a standard two-level 400 Hz GPU. The implementation includes third, fifth, and seventh order harmonic compensation but cannot be reasonably extended to higher order harmonics, such as 11th (4.4 kHz), 13th (5.2 kHz), or 15th (6 kHz) as the power losses of the converter limit the switching frequency and therefore, the higher order harmonic compensation. Furthermore, no stability analysis has been undertaken in [5].

The contributions of this paper can be summarized as follows.

1) A simple methodology for designing a single-loop resonant controller with multiple resonances, for regulation of the fundamental 400 Hz voltage signal as well as compensation of high-order harmonic components, under nonlinear and unbalanced loads, is proposed and successfully validated. The methodology allows direct design of one controller with multiple resonances, avoiding the superposition of individually designed resonant controllers as presented in [16] and[17]. Multiple dq frame transformations and positive–negative sequence decomposition are avoided, which is an important advantage over other published methods [18], [19].

2) The proposed methodology can be used to design a robust and more stable control system when the sampling frequency is close to the Shannon–Nyquist frequency (theoretical limitation). This is important for a 400 Hz GPU application. An analytical design for the fully discretized controller based on Nyquist response, considering delay compensation is proposed in this paper and experimentally validated. This improves the stability and robustness, when a nondamped resonant LC output filter is implemented and the sampling frequency is close to the compensated harmonic components.

3) A four-leg three-level neutral point clamped (NPC) has been validated as a suitable solution for a 400 Hz GPU application. The multilevel nature of this topology increases the equivalent frequency of the modulated waveform compared to the switching frequency of each device, which is a major advantage for the GPU, allowing higher order harmonic compensation compared to the two-level voltage source inverter (VSI) typically reported in the literature [5], [13], [16]–[18]. The fourth leg of the converter provides a path for zero-sequence current

components, i.e., unbalanced loads, producing five-level phase-to-neutral output voltages which allow implementation of smaller output power filters with lower reactive power consumption [20].

The rest of this paper is organized as follows. In Section II, the proposed control methodology is introduced and extensively analyzed. Three-dimensional (3-D) modulation is discussed in Section III. Section IV concludes this paper.

II. SINGLE-LOOP VOLTAGE CONTROL STRATEGY

Resonant controllers and rotating dq controllers are the most suitable alternatives for single-loop voltage control of grid connected and stand alone power converters [13], [21]–[23]. Both schemes provide good transient and steady-state performance. However, when unbalanced and harmonic compensation are required, resonant controllers are simpler to design and require less computational burden. They avoid multiple reference frame transformations and positive/negative sequence separation, and give direct control over the zero-sequence present in four-wire systems.

Fig. 1 shows the proposed solution for a 400 Hz, 110 V GPU, where the aircraft represents a linear/nonlinear, balanced/unbalanced load. A small LC filter is used at the output of the converter. A single-loop resonant controller controls the output voltage of the GPU, compensating the third, fifth, seventh, ninth, and eleventh harmonics. A 3-D space vector modulation (SVM) algorithm in $\alpha\beta\gamma$ coordinates is used to synthesize the output voltages [24]. Furthermore, using the redundant vectors of the four-leg NPC and output current measurements, a proportional-integral (PI) controller is used to balance the voltage on the dc-link capacitors.

The transfer function of the second-order LC filter shown in Fig. 1 is

$$P(s) = \frac{V_o(s)}{V_i(s)} = \frac{1}{L_f C_f s^2 + R_f C_f s + 1} \qquad (1)$$

where L_f, R_f, and C_f represent the parameters of the LC filter.

The resonant controller design must provide sufficient stability margins for each of the compensated harmonics. Hence, the controller is implemented with angle compensation with a transfer function given by

$$G^c(s) = \sum_{n=1}^{k} R_n^c(s) = \sum_{n=1}^{k} K_n \frac{s \cos \vartheta_n - \omega_n \sin \vartheta_n}{s^2 + \omega_n^2} \qquad (2)$$

where K_n represents the gain and ω_n is the resonance frequency for the nth resonant compensator. Furthermore, the phase of each compensator can be modified by adjusting ϑ_n. Setting this angle as $\vartheta_n = -\angle P_d(j\omega_n)$ compensates the phase shift injected by the plant, giving an open-loop phase shift of $\pm 90°$ around the resonance frequencies and increasing the stability margin of the closed-loop system.

Notice that ϑ_n compensates both the phase shift introduced by the plant (at the resonant frequencies ω_n) and also the loss of phase margin produced by the one-sample time delay introduced by the SVM algorithm.
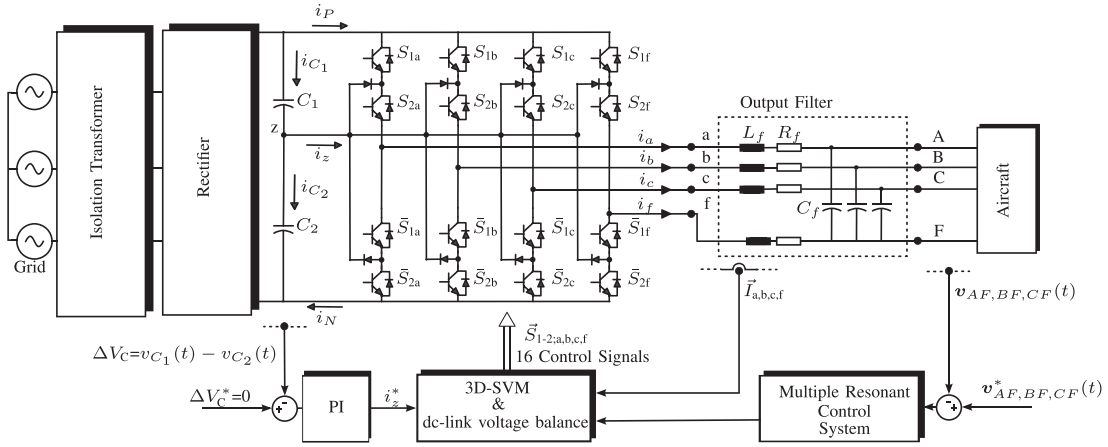
Fig. 1. Control scheme for the proposed four-leg NPC converter used as GPU. An small output LC filter is used to obtain 400 Hz sinusoidal output voltages. R_f represents the series resistance, L_f is the filter inductance, and C_f is the capacitor of the filter.
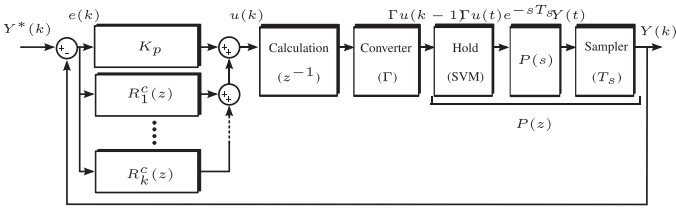

Fig. 2. Discrete-time single-loop control structure for the implementation of resonant controllers. $Y^*(k)$ and $Y(k)$ represent the reference and controlled discrete-time variables. $R_n^c(z)$ for $n = \{1, 2, \ldots, k\}$ represents a resonant controller with delay compensation for compensation of a signal with frequency ω_n in discrete time.

A. Discrete Time Representation

To implement the controller in a digital platform, a discrete-time representation and design for the controller and the plant are required. Fig. 2 presents the discrete-time control scheme of a resonant controller implemented for a second-order system. The control algorithm calculation time is represented as a unit delay and the VSI is represented as a constant gain.

For the SVM algorithm, the output voltages of the LC filter are measured at every sampling time T_s. Furthermore, the output voltages of the converter are maintained constant during each sampling time T_s. Therefore, the plant can be considered as a continuous system cascaded with a zero-order hold (ZOH) circuit and a sampled output. Thereby, the ZOH discrete representation (see [15]) of the second-order system of (1) is given by

$$P^{\text{zoh}}(z) = 1 - \tag{3}$$

$$\frac{z-1}{\sqrt{1-\xi^2}} \left(\frac{ze^{-\xi\omega_{\text{nat}}T_s}\sqrt{1-\xi^2}\sin\left(T_s\omega_{\text{nat}}\sqrt{1-\xi^2} - \arccos(\xi)\right)}{z^2 - 2ze^{-\xi\omega_{\text{nat}}T_s}\cos\left(T_s\omega_{\text{nat}}\sqrt{1-\xi^2}\right) + e^{-2\xi\omega_{\text{nat}}T_s}} \right)$$

$$\omega_{\text{nat}} = \frac{1}{\sqrt{L_f C_f}} \tag{4}$$

$$\xi = \frac{R_f\sqrt{L_f C_f}}{2L_f}. \tag{5}$$

To ensure zero steady-state error to sinusoidal reference signals, the discretization method applied to (2) must maintain the resonant frequencies ω_n unaltered, providing infinite gain at each of these frequencies [13], [14]. Accordingly, the first-order hold (FOH) and Tustin with prewarping (TPW) methods, setting the prewarping frequency as each ω_n, are suitable approximations of the continuous system. Thus, using the FOH approximation, the discrete form of the resonant controller of (2) is given by

$$R^{c-\text{foh}}(z) = \sum_{n=1}^{k} K_n \frac{\cos(\omega_n D_n T_s)(1-z^{-2})(1-\cos(\omega_n T_s)))}{\omega_n^2 T_s(1 - 2z^{-1}\cos(\omega_n T_s) + z^{-2})} -$$

$$\frac{\sin(\omega_n D_n T_s)\left[\omega_n T_s - \sin(\omega_n T_s) + 2z^{-1}\sin(\omega_n T_s)\right]}{\omega_n^2 T_s(1 - 2z^{-1}\cos(\omega_n T_s) + z^{-2})} -$$

$$\frac{\sin(\omega_n D_n T_s)[-2z^{-1}\omega_n T_s\cos(\omega_n T_s) + z^{-2}(\omega_n T_s - \sin(\omega_n T_s))]}{\omega_n^2 T_s(1 - 2z^{-1}\cos(\omega_n T_s) + z^{-2})} \tag{6}$$

where T_s is the sampling time used for the discretization and ω_n is the resonance frequency of the nth resonant controller. The term D_n represents the number of samples required for compensating the phase shift introduced by the plant. Equivalent to ϑ_n of (2), D_n for the nth resonant controller is given by

$$D_n = \frac{-\angle P^{\text{zoh}}(z_n = e^{j\omega_n T_s})\text{rad}}{T_s\omega_n} \tag{7}$$

where $P^{\text{zoh}}(z_n = e^{j\omega_n T_s})$ represents the ZOH discrete-time representation of (3) evaluated at the resonance frequency ω_n.

B. Controller Design

Different strategies have been proposed in the literature for the design of resonant controllers employing Nyquist diagrams [13], [16]–[19]. However, these approaches usually use a first-order plant or make a first-order approximation, neglecting the resonant effect of a higher order filter. This allows independent design for each resonant compensator, which can be useful when the resonance of the filter is far from the resonance of each
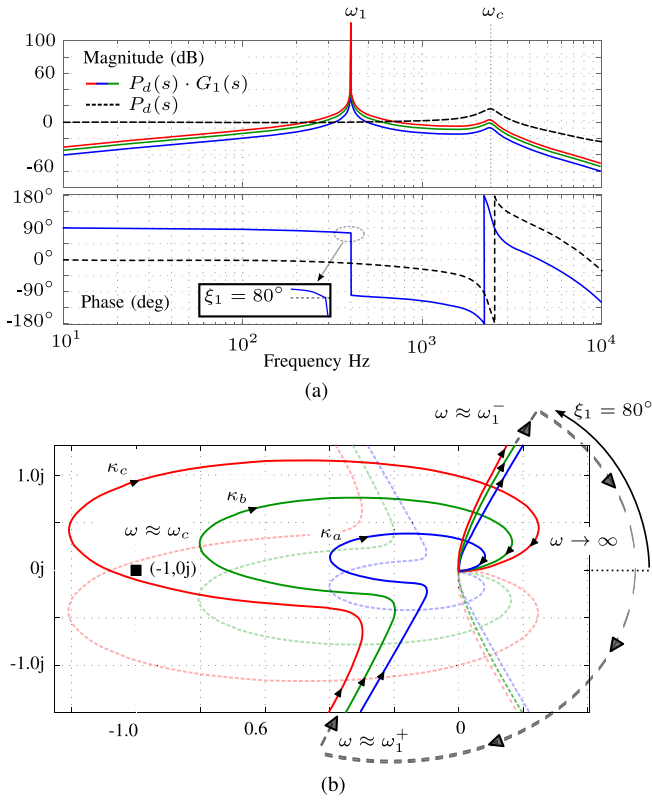
Fig. 3. (a) Bode and (b) Nyquist diagrams for the open-loop system $H_1(s) = G_1(s)P_d(s)$. $P_d(s) = P(s) \cdot e^{-sT_s}$, $T_s = 1/16800$ s, $P(s)$, with $R_f = 0.5\ \Omega$, $L_f = 219\ \mu$ H, and $C_f = 20\ \mu$F posses a resonance at $\omega_c \approx 2\pi \cdot 2400$ rad/s. $G_1(s) = K_1 \frac{s}{s^2 + \omega_1^2}$, $\omega_1 = 2\pi \cdot 400$ rad/s and three different gains have been used $K_{1a} = 1000$, $K_{1b} = 2000$, and $K_{1c} = 3000$. In (b), $\kappa_{a,b,c}$ represents the Nyquist plot for the gains $K_{1a,1b,1c}$, the dotted semitransparent lines represent the Nyquist response for negative frequencies.

compensator. However, when high-order harmonics relatively close to the resonance of the filter have to be compensated, an independent design of each compensator can lead to instability. Therefore, a design considering all the resonant compensators in a single transfer function is required and studied in this section.

Fig. 3 shows the Bode and Nyquist response for the open loop system $H_1(s) = G(s)P(s)e^{-sT_s}$, considering the resonant controller of (2), tuned only at the fundamental 400 Hz frequency with $\vartheta_1 = 0°$, and the second-order filter of (1). Fig. 3(a) shows the bode plot of $H_1(s)$ for three different gains $K_{1a,1b,1c}$ including a sampling time delay T_s. The later introduces a phase shift of $-10°$ at ω_1, and the phase of $H_1(s)$ steps from $\xi_1 = 80°$ to $\xi_1 - 180°$ at ω_1. Fig. 3(b) shows the Nyquist diagram of $H_1(s)$ for the three different gains $K_{1a,1b,1c}$. The Nyquist diagram starts from the point $(0, 0j)$ at $\omega = 0$ rads^{-1}; as ω approaches from 0 to ω_1, the magnitude of $H_1(s)$ increases toward infinity with an angle ξ_1. After $\omega > \omega_1$, the phase of the Nyquist plot turns rapidly through $180°$ to appear from the bottom of the frame. Thereafter, instead of directly approaching zero, the Nyquist plot describes a curve which approaches the left side of the plane, making it possible to enclose the critical stability point $(-1, 0j)$. This curve is produced by the resonance of the second-order filter ω_c, defining the stability margin of the

closed-loop system and representing a constraint for the gain of the controller in order to maintain closed-loop stability. From Fig. 3(b), the curve κ_c leads to an unstable system, nevertheless the phase margin of the open loop system, before the resonance peak is $\approx 90°$. This shows one of the problems of Bode diagrams in designing resonant control systems, especially when multiple resonant controllers are implemented. There are many frequencies where the magnitude of $G(s)H(s)$ crosses the 0 db line (e.g., see Fig. 5). Therefore, it is difficult to predict the performance and overall stability using a Bode diagram and phase margins, in control systems where multiple resonant controllers are implemented. For this reason, Nyquist diagrams are preferred in this paper, because they have significant advantages for the design of high-order controllers with multiple resonant peaks.

Additionally, from Fig. 3(b) it is concluded that for an angle $\xi_1 < 0$, the Nyquist path would enclose the point $(-1, 0j)$ regardless of the controller gain. This is of particular importance when high-order harmonics have to be compensated, as the phase of the open loop system rapidly decreases as a result of the phase injected by the sampling delay $P_d(s) = P(s)e^{-sT_s}$. Thereby, to increase the stability margin of the closed-loop system, it is desirable to set ξ_1 to $90°$ at the resonance frequency ω_1. Thereby, to set each angle ξ_n to $90°$, the phase shift produced by the plant at each resonance frequency $\vartheta_n = -\angle P_d(j\omega_n)$ has to be compensated in (2).

Fig. 4(a) shows the open-loop bode diagram of $H_1^c(s) = P_d(s)G_1^c(s)$ considering a resonant controller to regulate the 400 Hz fundamental, including the phase compensation. The phase shift is now $\pm 90°$ at the resonance frequency ω_1. Similar to Fig. 3(b), Fig. 4(b) shows the Nyquist diagram for the open-loop system considering phase compensation ($H_1^c(s)$). The introduction of the phase-shift compensation allows placement of the asymptotes parallel to the $j\omega$ axis ($\xi_1 = 90°$), which helps maintain the stability of the closed-loop system when high frequencies are compensated. The paths σ_1 and σ_2 show the trajectory of the Nyquist response as ω approaches the resonance frequency ω_1. Additionally, the magnitude of the closed-loop frequency response, i.e., M circle tangent to the Nyquist response, has been plotted in order to set the gain of the controller K_1 for obtaining a damping factor of $\zeta = 0.65$. The damping factor ζ and the magnitude of the closed-loop frequency response are related by [15]

$$M \approx \frac{1}{2\zeta\sqrt{1 - \zeta^2}}. \qquad (8)$$

Fig. 5 shows the Bode and Nyquist diagrams for the open-loop system composed of $P_d(s)$ and a resonant voltage controller to regulate not only the fundamental 400 Hz frequency, but to eliminate all the odd harmonics up to the eleventh. As expected, Fig. 5(a) possesses six resonant peaks at the frequencies $\omega_{1,3,5,7,9,11}$ with $\pm 90°$ phase shift around the resonance frequencies. The phase compensation places the asymptotes, for each resonance frequency $\omega_{1,3,5,7,9,11}$, parallel to the $j\omega$ axis in the Nyquist diagram of Fig. 5(b), which reduces the possibility of enclosing the critical point $(-1, 0j)$. Equivalent to Fig. 4(b), from Fig. 5(b) a set of paths σ_1 to σ_{12} can be recognized. The
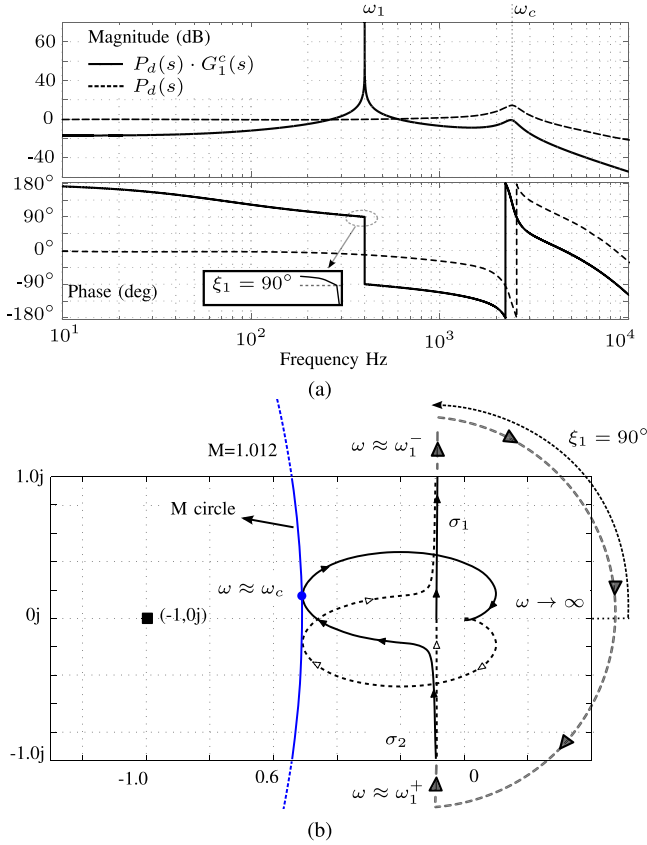
Fig. 4. (a) Bode and (b) Nyquist diagram for the open-loop system $H_1^c(s) = G_1^c(s)P_d(s)$. $P_d(s) = P(s) \cdot e^{-sT_s}$, $T_s = 1/16800$ s, $P(s)$, with $R_f = 0.5\Omega$, $L_f = 219$ μH, and $C_f = 20$ μF posses a resonance at $\omega_c = 2\pi \cdot 2400$ rad/s. $G_1(s) = K_1 \frac{s\cos\vartheta_1 - \omega_1 \sin\vartheta_1}{s^2 + \omega_1^2}$, $\omega_1 = 2\pi \cdot 400$ rad/s, $\vartheta_1 = -10°$, $K_1 = 1255$. In (b), Nyquist response for positive and negative frequencies (dotted lines) is shown. The tangent *M* circle for $M = 1.01, 2$ is centred at $(-42.41,0j)$ with a radius of 41.91 and associated with a damping factor of $\zeta = 0.65$.

frequency increases starting from 0 Hz along the trajectory described by σ_1, the magnitude of the Nyquist plot increases to infinity (with an angle of 90°) at the resonant frequency ω_1, thereafter the plot moves to the bottom of the diagram with an angle of $-90°$ (trajectory σ_2). Similar trajectories are produced for each resonant frequency, thus, σ_3–σ_4 for ω_3, σ_5–σ_6 for ω_5, etc. Although the gain of each compensator of $G_{1,3,5,7,9,11}^c(s)$ contributes to driving the Nyquist plot toward the critical point $(-1,0j)$, the gains K_5 and K_7 have to be well-limited as their associated peaks are closer to ω_c. Table I summarizes the angles injected by the plant and the computational delay in order to compensate ϑ_n in each compensator. Additionally, the path σ_n of Fig. 5 related to each resonance frequency is also depicted.

III. 3-D SPACE VECTOR MODULATION

To generate the voltage demanded by the multiple resonant controllers, the 3-D SVM presented in [24] and [25] has been used. Fig. 6 shows the three-dimensional modulation space, where the reference vector can be modulated. This space is
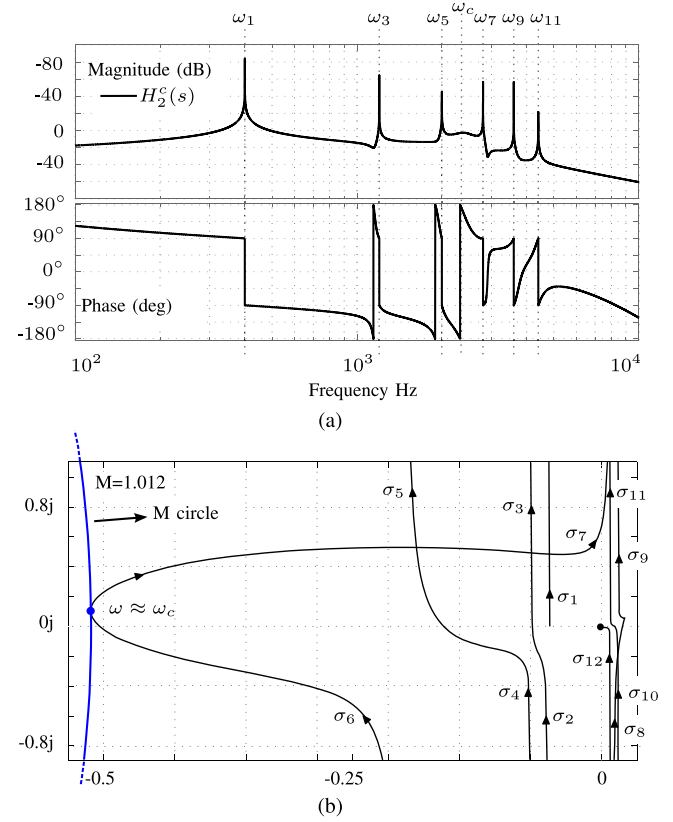

Fig. 5. (a) Bode and (b) Nyquist diagrams for the open-loop system $H_2^c(s) = G_{1,3,5,7,9,11}^c(s)P_d(s)$. $P_d(s) = P(s) \cdot e^{-sT_s}$, $T_s = 1/16800$ s, $P(s)$, with $R_f = 0.5$ Ω, $L_f = 219$ μH, and $C_f = 20$ μF posses a resonance at $\omega_c = 2\pi \cdot 2400$ rad/s. $G_{1,3,5,7,9,11}(s) = \sum_{n=1,3,5,7,9,11}^{1} K_n \frac{s\cos\vartheta_n - \omega_n\sin\vartheta_n}{s^2 + \omega_n^2}$, $\omega_1 = 2\pi \cdot 400$ rad/s, $\omega_3 = 3\omega_1$ rad/s, $\omega_5 = 5\omega_1$ rad/s, $\omega_7 = 7\omega_1$ rad/s, $\omega_9 = 9\omega_1$ rad/s, and $\omega_{11} = 11\omega_1$ rad/s. $K_1 = 610$, $K_{3,5,7,9,11} = 80$. In (b), Nyquist response for only positive frequencies is shown. The paths σ_1 to σ_n show the trajectory of the Nyquist response as $\omega \approx \omega_n^-$ and $\omega \approx \omega_n^+$ for each resonance frequency. The tangent *M* circle for $M = 1.012$ is centred at $(-42.41,0j)$ with a radius of 41.91 and associated to a damping factor of $\zeta = 0.65$.

TABLE I
ANGLE COMPENSATION ϑ_n FOR $G_{1,3,5,7,9,11}^c(s)$

R_n^c & σ_n	ω_n rad/s	$-\angle P(j\omega_n)$	$-\angle e^{-j\omega_n T_s}$	ϑ_n
$R_1^c(s)$ (σ_1, σ_2)	$2\pi \cdot 400$	$1.48°$	$8.57°$	$10.05°$
$R_3^c(s)$ (σ_3, σ_4)	$2\pi \cdot 1200$	$5.73°$	$25.71°$	$31.44°$
$R_5^c(s)$ (σ_5, σ_6)	$2\pi \cdot 2000$	$22.17°$	$42.85°$	$65.03°$
$R_7^c(s)$ (σ_7, σ_8)	$2\pi \cdot 2800$	$153.68°$	$60°$	$213.68°$
$R_9^c(s)$ (σ_9, σ_{10})	$2\pi \cdot 3600$	$169.67°$	$77.14°$	$246.81°$
$R_{11}^c(s)$ $(\sigma_{11}, \sigma_{12})$	$2\pi \cdot 4400$	$173.28°$	$94.28°$	$267.56°$

formed by 65 different vectors, where 14 vectors posses one redundancy and the zero vector possesses two redundancies, making up the $3^4 = 81$ switching states of the converter. For simplicity, only 14 vectors that shape the modulation region, are represented in Fig. 6. The reference vector $v_{\alpha\beta\gamma}^*$ is also depicted inside the modulation space. To obtain the modulation space of the converter, each of the 81 switching states are transformed using the Clarke transform (see Appendix) as presented in
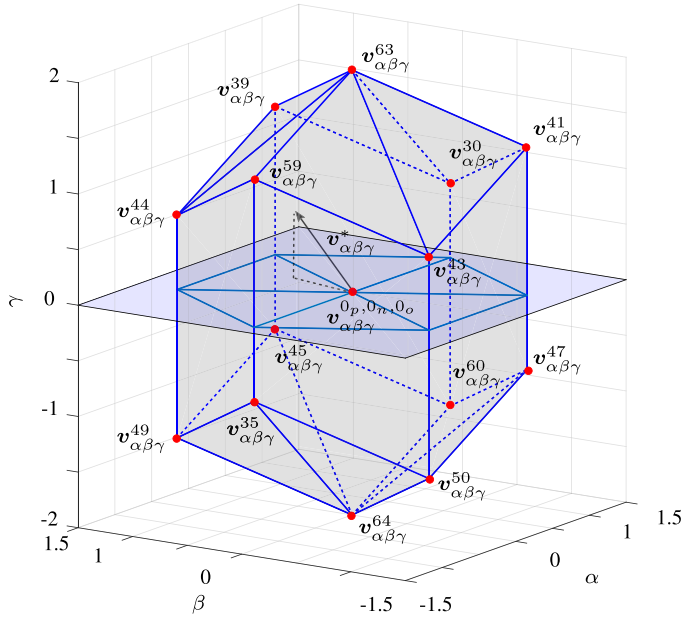
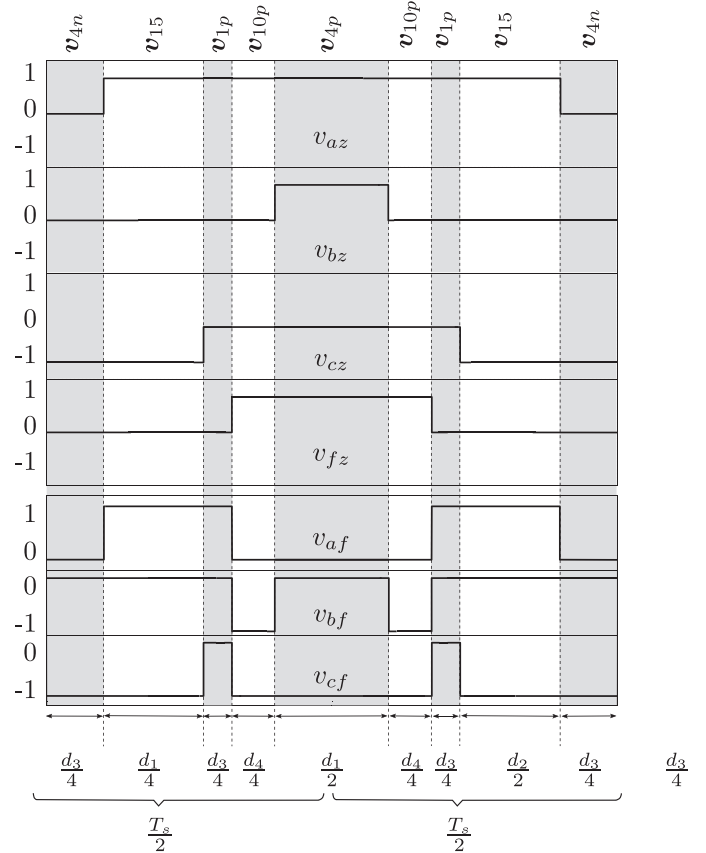Fig. 6. Modulation region for a three-level four-leg NPC converter.

Fig. 7. Switching commutation based on a single redundancy switching pattern. The vectors that compose the selected tetrahedron are: $\boldsymbol{v}_4$ ([OONO] or [PPOP]), $\boldsymbol{v}_{15}$ ([PONO]), $\boldsymbol{v}_1$ ([ONNN] or [POOO]), $\boldsymbol{v}_{10}$ ([ONNO] or [POOP]), where P, N, and O stands for positive, zero, or negative output voltage of each leg of the four-leg NPC converter.

(9)–(11). The voltages used in (10) are referred to Fig. 1

$$\boldsymbol{v}_{\alpha\beta\gamma}^i = \boldsymbol{T}_{abc}^{\alpha\beta\gamma} \boldsymbol{v}_{abc}^i \tag{9}$$

$$\boldsymbol{v}_{abc}^i = [v_{af}^i, v_{bf}^i, v_{cf}^i] \tag{10}$$

$$\boldsymbol{v}_{\alpha\beta\gamma}^* = \boldsymbol{T}_{abc}^{\alpha\beta\gamma} \boldsymbol{v}_{abc}^*. \tag{11}$$

The reference vector $\boldsymbol{v}_{\alpha\beta\gamma}^*$, presented in Fig. 6, can be placed anywhere inside the modulation region and is generated by selecting the four nearest vectors at each sampling time. Thus, the first step to achieve modulation is to identify the four vectors that form the tetrahedron that encloses the reference vector. This can be achieved by the following simple steps:

$$\boldsymbol{v}_{0_{\alpha\beta\gamma}} = \boldsymbol{T}_{abc}^{\alpha\beta\gamma} \boldsymbol{floor}\, (\boldsymbol{v}_{abc}^*) \tag{12}$$

$$\boldsymbol{v}_{0'_{\alpha\beta\gamma}} = \boldsymbol{v}_{0_{\alpha\beta\gamma}} + [0, 0, 1] \tag{13}$$

$$\hat{\boldsymbol{v}}_{\alpha\beta\gamma}^* = \boldsymbol{v}_{\alpha\beta\gamma}^* - \boldsymbol{v}_{0_{\alpha\beta\gamma}} = [\hat{v}_\alpha, \hat{v}_\beta, \hat{v}_\gamma] \tag{14}$$

$$\phi = \tan^{-1}\left(\frac{\hat{v}_\beta}{\hat{v}_\alpha}\right). \tag{15}$$

In (12) and (13), the first two vectors of the converter are selected, and then, similarly to the SVM algorithm for a two-level converter, based on the angle calculated on (15), the final two active vectors are selected, which are separated by 60° and have a constant amplitude. Thereafter, the duty cycles for each vector can be calculated as

$$\begin{bmatrix} d_2 \\ d_3 \\ d_4 \end{bmatrix} = \boldsymbol{D_n} \begin{bmatrix} \hat{\boldsymbol{v}}^*{}_\alpha \\ \hat{\boldsymbol{v}}^*{}_\beta \\ \hat{\boldsymbol{v}}^*{}_\gamma \end{bmatrix} \tag{16}$$

$$d_1 = 1 - d_2 - d_3 - d_4 \tag{17}$$

where d_1 to d_4 represent the duty cycle of each of the four vectors that modulate the reference vector and the matrix $\boldsymbol{D_n}$ takes six different values depending on the sector according to (15) (see Appendix).

A. Switching Sequence and Power Losses

After the stationary vectors and their dwell times have been obtained, a switching pattern that arranges these vectors during the sampling time T_s has to be defined. The selection of this pattern, also known as the switching sequence, is always a trade-off between the number of commutations, i.e., switching power losses, and the accuracy of tracking a reference signal, i.e., current or voltage ripple. Therefore, the selection between different patterns mostly depends on the application. In this paper, a single redundancy switching pattern is defined and implemented. This pattern uses only one of all the available redundant vectors at each sampling time. This reduces the switching frequency of the devices and also distributes the power losses uniformly among the devices. Fig. 7 shows an example of the commutation sequence for the modulation of a reference vector inside a tetrahedron formed by the vectors $\boldsymbol{v}_4$, $\boldsymbol{v}_{15}$, $\boldsymbol{v}_1$, and $\boldsymbol{v}_{10}$. Although vectors $\boldsymbol{v}_1$, $\boldsymbol{v}_4$, and $\boldsymbol{v}_{10}$ posses one redundancy, only the redundancy of the vector $\boldsymbol{v}_4$ has been used.

As shown in Fig. 7, regardless of the path described by the reference vector in Fig. 6, always one commutation takes place
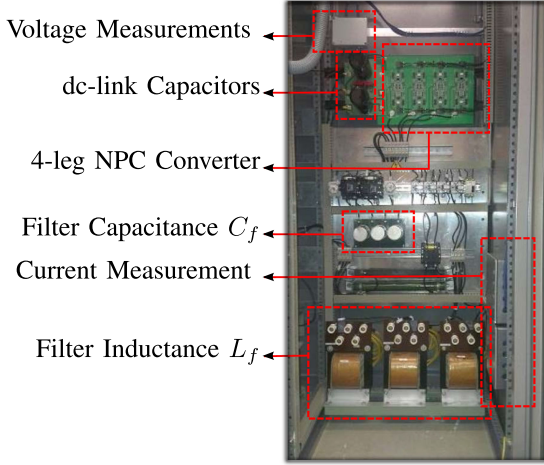
Fig. 8.   Experimental rig for a four-leg NPC converter.

TABLE II
GENERAL PARAMETERS OF THE IMPLEMENTED SYSTEMS

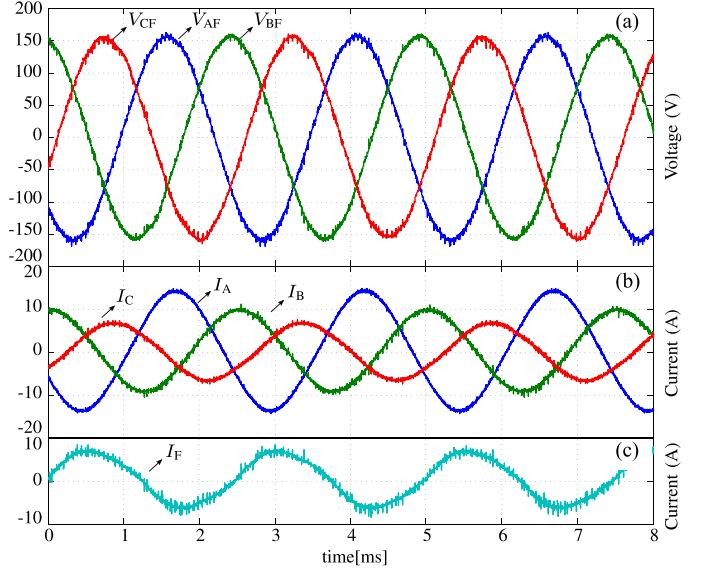| Parameter	Value	Parameter	Value
C_1	3300 uF	Z	$10\,\Omega$; $0.8\,mH$
C_2	3300 uF	Z_{a2}	$10\,\Omega$; $0.8\,mH$
V_{dc}	325 V	Z_{b2}	$14\,\Omega$; $0.8\,mH$
C_f	20 uF	Z_{c2}	$18\,\Omega$; $0.8\,mH$
L_f	219 uH	Single/Three-Phase Full Wave	$220\,uF$; $57\,\Omega$
f_{sw}	16.8 kHz	Diode Bridge Rectifier	

Fig. 9.   Performance of the proposed GPU under a 2.8 kW, linear-unbalanced load (Z_{a2}, Z_{b2}, Z_{c2}). Sampling frequency of $f_s = 16.8$ kHz. (a) Output voltages V_{AF}, V_{BF}, V_{CF}, (b) line currents I_A, I_B, I_C and (c) neutral wire current I_F.

at every sampling time. Thereby, considering that ac signals are being modulated, the switching frequency per device over a fundamental cycle in a four-leg NPC converter, is given by

$$\bar{f}_{\text{dev}} = \frac{f_s}{2} \qquad (18)$$

where f_s represents the sampling frequency and $\bar{f}_{\text{dev}}$ is the average switching frequency of each of the four switching devices of each leg of the converter. The equivalent switching frequency of the output voltage is still f_s. This is an important advantage compared with a two-level inverter, where the switching frequency of each device is equal to the equivalent frequency of the modulated waveform, i.e., f_s.

IV. EXPERIMENTAL VALIDATION

The experimental rig used to validate the proposed controller in a four-leg NPC is illustrated in Fig. 8 (load is not shown). The control system hardware is composed of a Pentium-System board (3.2 GHz Pentium processor, 2 GB RAM host PC, based on the Arch-Linux operating system) and an field-programmable gate array (FPGA) board connected via an ISA-bus. This platform runs the algorithm using the real time application interface (RTAI) for Linux. The FPGA board manages the ADCs, implements the overvoltage and overcurrent protections, performs the dead time, and generates the insulated-gate bipolar transistor (IGBT) switching signals. Optical fibers are used to transmit the IGBT gate signals from the FPGA output buffer to the NPC converter.

A four-leg NPC converter has been designed based on the Microsemi IGBT-APTGL60TL120T3G rated at 60 A and 1200 V. The nominal power of the experimental prototype is 6 kVA. The experimental results presented in this section utilize step impacts and steady-state connection of linear/nonlinear unbalanced loads in order to verify the performance of the prototype and its capacity to fulfill the standards of [2].

A. Experimental Results

In order to validate the proposed topology and control design, the aircraft of Fig. 1 is replaced by linear/nonlinear,

balanced/unbalanced loads in the experimental rig. The steady-state and transient performance is investigated in the following sections. Table II gives the common parameters used for the experimental results.

1) Steady-State Performance: Fig. 9 shows the performance of the proposed system of Fig. 1 under unbalanced operation, using Z_{a2}, Z_{b2}, and Z_{c2}. The power consumption of each branch is 1.21, 0.86, and 0.67 kW, respectively. As depicted in Fig. 1, the controller compensates the different voltage drops on each phase of the filter and maintains the output voltages at 110 V, 400 Hz. The neutral current has a reduced harmonic distortion due to cancellation of some of the harmonic components in the line currents. The THDs of each output voltage are 0.87, 0.92, and 1.10%, respectively, which easily meets the maximum of 5% required by the standard [2].

In order to evaluate the performance of the proposed topology and control strategy when feeding nonlinear loads, a three-phase and a single-phase full wave diode bridge rectifier, both with an RC load at the dc side, are connected at the output of the GPU (see Table II). Fig. 11 shows the reference voltage generated by the controller, which is then synthesized by the 3D-SVM [24], [25]. Clearly, the reference voltage is far from an ideal sinusoidal shape. However, this is the required waveform to compensate the harmonic voltage drop produced by the distorted current circulating through the filter inductance L_f to subsequently obtain
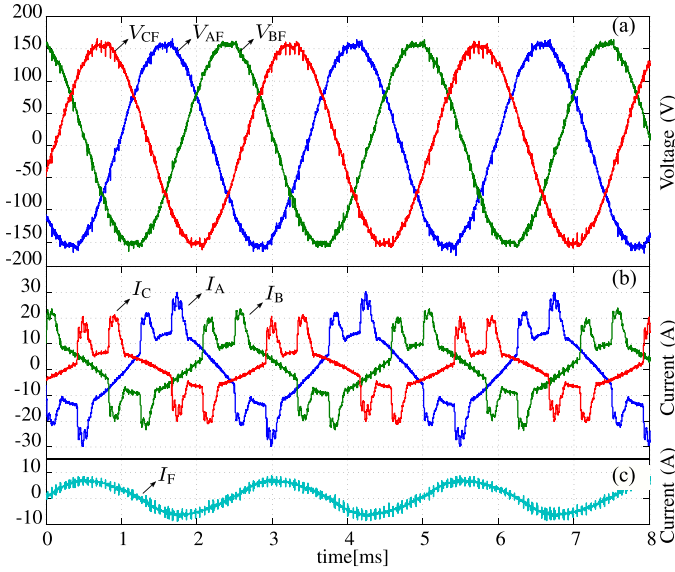
Fig. 10. Performance of the proposed GPU under a 2.8 kW linear-unbalanced load (Z_{a2}, Z_{b2}, Z_{c2}) and a 1.27 kW three-phase full wave diode bridge rectifier (57 Ω and 220 μF). Sampling frequency of f_s = 16.8 kHz. (a) Output voltages V_{AF}, V_{BF}, V_{CF}, (b) line currents I_A, I_B, I_C, and (c) neutral wire current I_F.
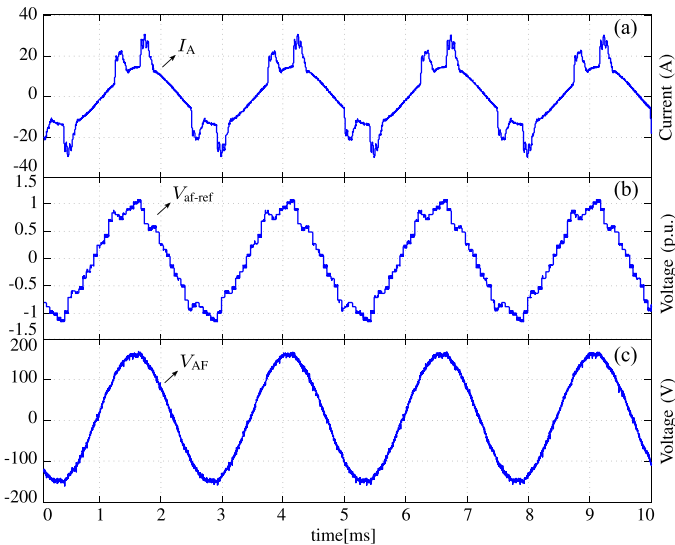

Fig. 11. Performance of the proposed GPU under a 2.8 kW linear-unbalanced load (Z_{a2}, Z_{b2}, Z_{c2}) and a 1.27 kW three-phase full wave diode bridge rectifier (57 Ω and 220 μF). Sampling frequency of f_s = 16.8 kHz. (a) Line current I_A, (b) reference voltage for the converter $V_{af\text{-}ref}$, and (c) GPU output voltage V_{AF}.

a sinusoidal voltage at the load. To highlight the effectiveness of the high-order harmonic compensation of the proposed method, output voltages and currents of the proposed GPU, considering only compensation of 400 Hz fundamental waveform, are shown in Fig. 12. As a result, highly distorted output voltages are obtained, with a THD$_v$ of 9.8% on each phase approximately.

Finally, Fig. 13 shows the performance of the proposed GPU for a test using a 0.42 kW single-phase full wave diode bridge rectifier and a 2.8 kW linear-unbalanced load (Z_{a2}, Z_{b2}, Z_{c2}). As the single-phase full wave diode bridge rectifier introduces
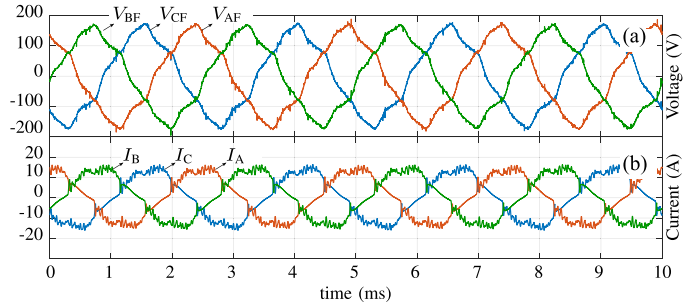

Fig. 12. Performance of the proposed GPU under a 2.5 kW linear-balanced load (Z) and a 1.27 kW three-phase full wave diode bridge rectifier (57 Ω and 220 μF). Compensation of only fundamental 400 Hz component (f_s = 16.8 kHz). (a) Output voltages V_{AF}, V_{BF}, and V_{CF} and (b) output currents I_A, I_B, I_C. $THD_V \approx 9.8\%$.
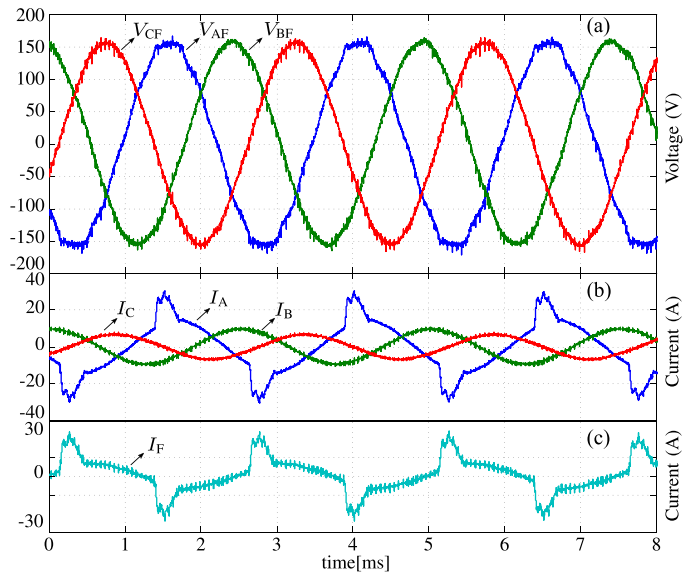

Fig. 13. Performance of the proposed GPU under a 2.8 kW linear-unbalanced load (Z_{a2}, Z_{b2}, Z_{c2}) and a 0.42 kW three-phase full wave diode bridge rectifier (57 Ω and 220 uF). Sampling frequency of f_s = 16.8 kHz. (a) Voltages V_{AF}, V_{BF}, V_{CF}, (b) line currents I_A, I_B, I_C, and (c) neutral wire current I_F.

a distorted zero-sequence component, the neutral current is not sinusoidal and contains the harmonics generated by the rectifier. This current also contains some even harmonics which are not compensated by the controller. Hence, although the THD is within the required limit for each phase (3.07, 1.2, and 1.2%, respectively), the phase where the single-phase rectifier is connected has the highest harmonic distortion.

2) Transient Performance: Fig. 14 illustrates a transient from unbalanced operation to a fully balanced load, while Fig. 15 shows a load impact from nominal balanced load to open circuit (the parameters of the load step are given in Table II). In both cases the controller achieves a good dynamic response, compensating the transient after approximately 1–2 cycles (2.5–5 ms), easily meeting the transient requirements in [2]. Fig. 16 shows the regulation of the voltages on the dc-link capacitors after a load impact from no-load condition to the 2.8 kW linear-unbalanced load. The voltage deviation is lower than
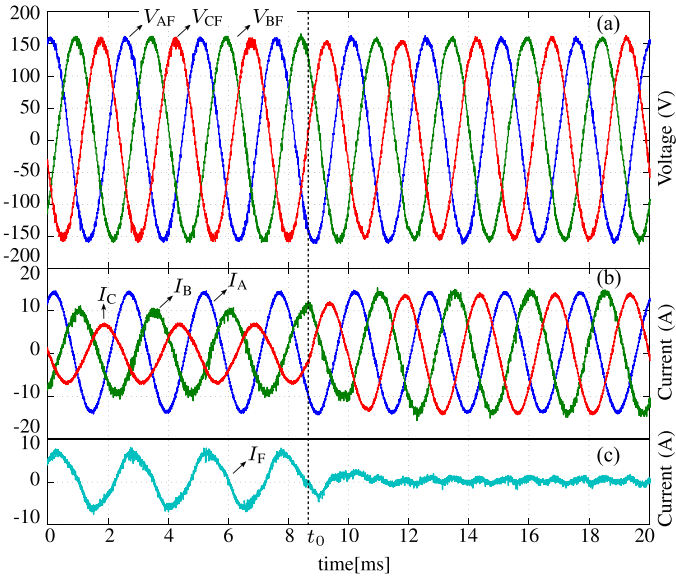
Fig. 14. Transient response of the proposed GPU for a load step from a 2.8 kW unbalanced load to a 3.6 kW balanced load. (a) Output voltages V_{AF}, V_{BF}, V_{CF}, (b) line currents I_A, I_B, I_C, and (c) the neutral wire current I_F.
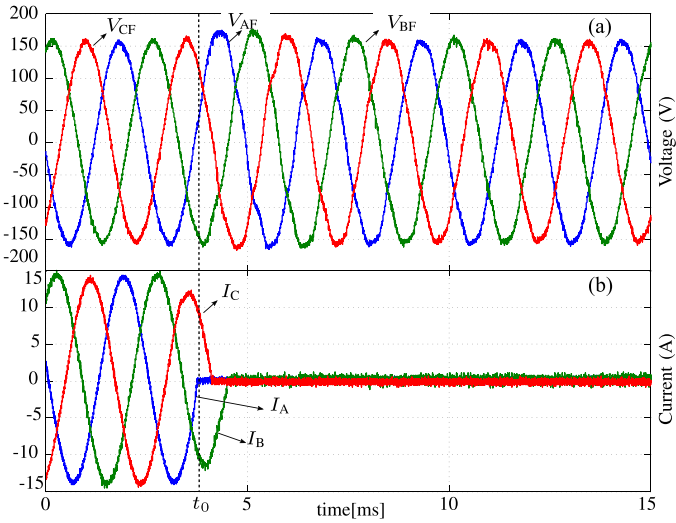

Fig. 15. Transient response of the proposed GPU for a load step from 3.6 kW balanced load to open circuit. (a) Output voltages V'_{AF}, V_{BF}, V_{CF} and (b) line currents I_A, I_B, I_C.
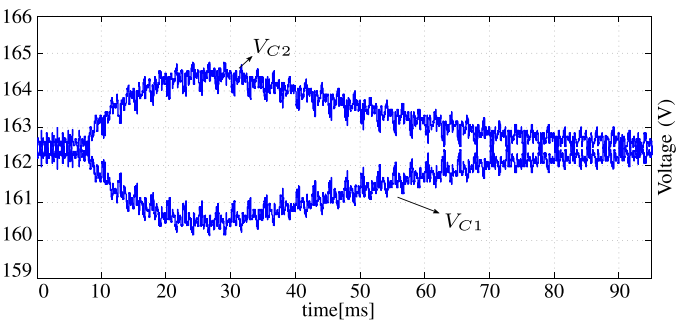

Fig. 16. Voltage of each capacitor of the dc-link after load step from open circuit to a 2.8 kW unbalanced load. The capacitors return to a balanced condition after the transient.
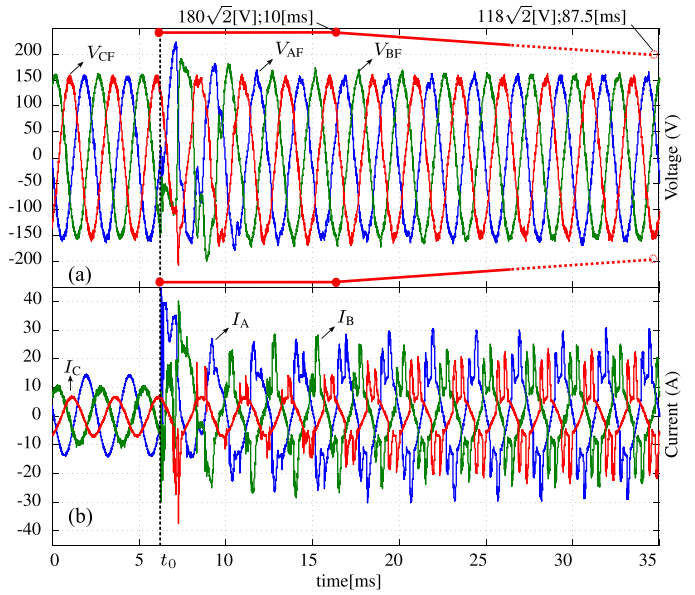

Fig. 17. Transient response of the proposed GPU for a 1.27 kW three-phase full wave diode bridge rectifier load impact from a 2.8 kW unbalanced load. (a) Output voltages V_{AF}, V_{BF}, V_{CF} and (b) line currents I_A, I_B, I_C.

5 V, converging to the reference after around 60 ms. This validates the effectiveness of the voltage balance algorithm used on the 3-D-SVM and the appropriate design of the PI controller utilized for balancing the voltage on each capacitor [24], [25].

Fig. 17 presents the transient response for a 1.27 kW load impact connected at the output of a three-phase full wave diode bridge rectifier. Even when considering that this is a large load impact, the controller can reject this disturbance after approximately 10 ms (3–4 cycles). As the capacitor is not charged before the load impact, it behaves as a short circuit and the voltage is not controllable for around a cycle. Additionally, the upper and lower transient boundaries of the standard are also depicted in Fig. 17(a) to highlight that the transient response easily meets the required standard [2], which allows an over voltage of 118 V after 87.5 ms.

V. CONCLUSION

This paper proposed a simple methodology to design multiple resonant controllers for high-order harmonic compensation when a small ratio between sampling frequency and harmonic compensated frequencies was required. Unlike previous methodologies, the work proposed in this paper did not assumed decoupled operation of the resonant controllers, taking into consideration the full dynamic of the plant and controllers. The method was based on Nyquist diagrams and it also allowed the design of multiple resonant controllers when a second-order output filter was used at the GPU output. This methodology overcomes typical difficulties associated with Bode design methods for high-order controllers with multiple resonant peaks. In addition, it overcame the problem of designing resonant controllers when the resonance frequency was close to the filter resonance frequency.

In order to achieve high-order harmonic compensation at 400 Hz fundamental waveform, a four-leg NPC converter was proposed as a solution. Thus, a double equivalent output frequency compared to the switching frequency per device was obtained. This allowes the use of smaller power filters, lower switching losses, and higher harmonic compensation. A resonant controller designed to regulate a fundamental signal of 400 Hz and eliminated the third, fifth, seventh, ninth, and 11th harmonics from the load voltage were successfully designed and experimentally validated.

Experimental results were conducted in a 6 kW prototype to validate the proposed methodology in a GPU application. The converter was tested under unbalanced and nonlinear loads performing excellent results maintaining sinusoidal output voltages under transient and steady-state operation. Furthermore, it was also demonstrated that dc-link voltage balancing could also be achieved even in the presence of severely unloaded nonlinear load.

APPENDIX

$$\boldsymbol{T}_{abc}^{\alpha\beta\gamma} = \frac{2}{3} \begin{bmatrix} 1 & -1/2 & -1/2 \\ 0 & \sqrt{3}/2 & -\sqrt{3}/2 \\ 1/2 & 1/2 & 1/2 \end{bmatrix} \tag{19}$$

The matrix $\boldsymbol{D}_n$ can be expressed for each interval as $\phi \in \left[\frac{(n-1)\pi}{3}, \frac{n\pi}{3}\right[\,; n \in \{1,2,3,4,5,6\}$

$$\boldsymbol{D}_1 = \begin{bmatrix} \frac{3}{2} & -\frac{\sqrt{3}}{2} & 0 \\ 0 & \sqrt{3} & 0 \\ -\frac{1}{2} & -\frac{\sqrt{3}}{2} & 1 \end{bmatrix} \boldsymbol{D}_4 = \begin{bmatrix} 0 & -\sqrt{3} & 0 \\ -\frac{3}{2} & \frac{\sqrt{3}}{2} & 0 \\ 1 & 0 & 1 \end{bmatrix}$$

$$\boldsymbol{D}_2 = \begin{bmatrix} -\frac{3}{2} & \frac{\sqrt{3}}{2} & 0 \\ \frac{3}{2} & \frac{\sqrt{3}}{2} & 0 \\ -\frac{1}{2} & -\frac{\sqrt{3}}{2} & 1 \end{bmatrix} \boldsymbol{D}_5 = \begin{bmatrix} -\frac{3}{2} & -\frac{\sqrt{3}}{2} & 0 \\ \frac{3}{2} & -\frac{\sqrt{3}}{2} & 0 \\ -\frac{1}{2} & \frac{\sqrt{3}}{2} & 1 \end{bmatrix} \tag{20}$$

$$\boldsymbol{D}_3 = \begin{bmatrix} 0 & \sqrt{3} & 0 \\ -\frac{3}{2} & -\frac{\sqrt{3}}{2} & 0 \\ 1 & 0 & 1 \end{bmatrix} \boldsymbol{D}_6 = \begin{bmatrix} \frac{3}{2} & \frac{\sqrt{3}}{2} & 0 \\ 0 & -\sqrt{3} & 0 \\ -\frac{1}{2} & \frac{\sqrt{3}}{2} & 1 \end{bmatrix}.$$

REFERENCES

[1] T. Wijekoon, L. Empringham, P. W. Wheeler, J. C. Clare, C. Whitley, and G. Towers, "Aircraft electrical landing gear actuation using dual-output power converter with mutual power circuit components," in *Proc. 24th Annu. IEEE Appl. Power Electron. Conf. Expo.*, 2009, pp. 1263–1268.

[2] *Aircraft Electric Power Characteristics*, MIL-STD-704F, Mar. 2004.

[3] *Ways of Dealing With Power Regeneration Onto an Aircraft Electrical Power System Bus*, AIR6139, SAE Int., Warrendale, PA, USA, Jan. 2014.

[4] U. B. Jensen, F. Blaabjerg, and J. K. Pedersen, "A new control method for 400-Hz ground power units for airplanes," *IEEE Trans. Ind. Appl.*, vol. 36, no. 1, pp. 180–187, Jan./Feb. 2000.

[5] Z. Li, Y. Li, P. Wang, H. Zhu, C. Liu, and F. Gao, "Single-loop digital control of high-power 400-Hz ground power unit for airplanes," *IEEE Trans. Ind. Electron.*, vol. 57, no. 2, pp. 532–543, Feb. 2010.

[6] M. K. Murugan, R. C. Eckenfelder, and J. Widdis, "Stepped waveform VSCF system with engine start capability," U.S. Patent 5 387 859A, Feb. 7, 1995.

[7] S. L. Arevalo, P. Zanchetta, P. W. Wheeler, A. Trentin, and L. Empringham, "Control and implementation of a matrix-converter-based ac ground power-supply unit for aircraft servicing," *IEEE Trans. Ind. Electron.*, vol. 57, no. 6, pp. 2076–2084, Jun. 2010.

[8] P. Wheeler, A. Trentin, S. Bozhko, and J. Clare, "Regeneration of energy onto an aircraft electrical power system from an electro-mechanical actuator," in *Proc. Elect. Syst. Aircr., Railway Ship Propulsion*, 2012, pp. 1–6.

[9] G. Escobar, A. A. Valdez, J. Leyva-Ramos, and P. Mattavelli, "Repetitive-based controller for a UPS inverter to compensate unbalance and harmonic distortion," *IEEE Trans. Ind. Electron.*, vol. 54, no. 1, pp. 504–510, Feb. 2007.

[10] P. Cortes, G. Ortiz, J. I. Yuz, J. Rodriguez, S. Vazquez, and L. G. Franquelo, "Model predictive control of an inverter with output LC filter for UPS applications," *IEEE Trans. Ind. Electron.*, vol. 56, no. 6, pp. 1875–1883, Jun. 2009.

[11] W. Rohouma, P. Zanchetta, P. W. Wheeler, and L. Empringham, "A four-leg matrix converter ground power unit with repetitive voltage control," *IEEE Trans. Ind. Electron.*, vol. 62, no. 4, pp. 2032–2040, Apr. 2015.

[12] R. Cardenas, C. Juri, R. Peña, P. Wheeler, and J. Clare, "The application of resonant controllers to four-leg matrix converters feeding unbalanced or nonlinear loads," *IEEE Trans. Power Electron.*, vol. 27, no. 3, pp. 1120–1129, Mar. 2012.

[13] A. G. Yepes, F. D. Freijedo, O. Lopez, and J. Doval-Gandoy, "Analysis and design of resonant current controllers for voltage-source converters by means of Nyquist diagrams and sensitivity function," *IEEE Trans. Ind. Electron.*, vol. 58, no. 11, pp. 5231–5250, Nov. 2011.

[14] A. G. Yepes, F. D. Freijedo, J. Doval-Gandoy, O. Lopez, J. Malvar, and P. Fernandez-Comesana, "Effects of discretization methods on the performance of resonant controllers," *IEEE Trans. Power Electron.*, vol. 25, no. 7, pp. 1692–1712, Jul. 2010.

[15] G. C. Goodwin, S. F. Graebe, and M. Salgado, *Control System Design*, 1st ed. Upper Saddle River, NJ, USA: Prentice-Hall, 2000.

[16] C. Lascu, L. Asiminoaei, I. Boldea, and F. Blaabjerg, "High performance current controller for selective harmonic compensation in active power filters," *IEEE Trans. Power Electron.*, vol. 22, no. 5, pp. 1826–1835, Sep. 2007.

[17] C. Lascu, L. Asiminoaei, and I. Boldea, "Frequency response analysis of current controllers for selective harmonic compensation in active power filters," *IEEE Trans. Ind. Electron.*, vol. 56, no. 2, pp. 337–347, Feb. 2009.

[18] S. Fukuda and T. Yoda, "A novel current-tracking method for active filters based on a sinusoidal internal model [for PWM invertors]," *IEEE Trans. Ind. Appl.*, vol. 37, no. 3, pp. 888–895, May/Jun. 2001.

[19] R. Bojoi, G. Griva, V. Bostan, M. Guerriero, F. Farina, and F. Profumo, "Current control strategy for power conditioners using sinusoidal signal integrators in synchronous reference frame," *IEEE Trans. Power Electron.*, vol. 20, no. 6, pp. 1402–1412, Nov. 2005.

[20] D. Floricau, G. Gateau, A. Leredde, and R. Teodorescu, "The efficiency of three-level active NPC converter for different PWM strategies," in *Proc. Power Electron. Appl.*, 2009, pp. 1–9.

[21] F. Blaabjerg, R. Teodorescu, M. Liserre, and A. V. Timbus, "Overview of control and grid synchronization for distributed power generation systems," *IEEE Trans. Ind. Electron.*, vol. 53, no. 5, pp. 1398–1409, Oct. 2006.

[22] F. Blaabjerg, Z. Chen, and S. B. Kjaer, "Power electronics as efficient interface in dispersed power generation systems," *IEEE Trans. Power Electron.*, vol. 19, no. 5, pp. 1184–1194, Sep. 2004.

[23] D. Zmood and D. Holmes, "Stationary frame current regulation of PWM inverters with zero steady-state error," *IEEE Trans. Power Electron.*, vol. 18, no. 3, pp. 814–822, May 2003.

[24] F. Rojas, R. Cárdenas, R. Kennel, J. C. Clare, and M. Díaz, "A simplified space-vector modulation algorithm for four-leg NPC converters," *IEEE Trans. Power Electron.*, vol. 32, no. 11, pp. 8371–8380, Nov. 2017.

[25] F. Rojas, R. Kennel, R. Cardenas, R. Repenning, J. C. Clare, and M. Diaz, "A new space-vector-modulation algorithm for a three-level four-leg NPC inverter," *IEEE Trans. Energy Convers.*, vol. 32, no. 1, pp. 23–35, Mar. 2017.

Félix Rojas (M'12) was born in Santiago, Chile. He received the B.Eng. and M.Sc. degrees in electrical engineering (Hons.) from the Universidad de Santiago de Chile, Santiago, in 2009, and the doctoral degree in electrical engineering from the Technical University of Munich, Munich, Germany, in 2015.

He is currently an Assistant Professor of Electrical Engineering with the Universidad de Santiago de Chile also a Research Associate with the Solar Energy Research Center (SERC Chile). His research interests are in control of power electronics converters for solar and wind energy conversion, power networks conditioning, high power electric vehicles chargers, and variable speed drives.

Matías Díaz (S'15) was born in Santiago, Chile. He received the B.Sc. and M.Sc. degrees in electrical engineering from the University of Santiago, Santiago, in 2011, and the dual Ph.D. degree in electrical and electronic engineering from the University of Nottingham, Nottingham, U.K., and the University of Chile, Santiago, in 2015.

He is Assistant Professor of Electrical Engineering in the Electrical Department of the Universidad de Santiago de Chile. His main research interests include the control of wind energy conversion systems and multilevel converters.

Roberto Cárdenas (S'95–M'97–SM'07) was born in Punta Arenas, Chile. He received the B.S. degree in electrical engineering from the University of Magallanes, Punta Arenas, Chile, in 1988, and the M.Sc. degree in modern electronics and the Ph.D. degree in electrical and electronics engineering from the University of Nottingham, Nottingham, U.K., in 1992 and 1996, respectively.

During 1989–1991 and 1996–2008, he was a Lecturer with the University of Magallanes. From 1991 to 1996, he was with Power Electronics Machines and Control Group, University of Nottingham. From 2009 to 2011, he was with the Electrical Engineering Department, University of Santiago, Santiago, Chile. He is currently a Professor of Power Electronics and Drives with the Electrical Engineering Department, University of Chile, Santiago, Chile. His main research interests include control of electrical machines, variable speed drives, and renewable energy systems.

Javier Pereda (S'09–M'14) received the B.Sc. (Eng.) (Hons.), M.Sc. and Ph.D. degrees in electrical engineering from the Pontificia Universidad Católica de Chile, Santiago, Chile, in 2007, 2009, and 2013, respectively.

Since 2013, he has been an Assistant Professor with the Department of Electrical Engineering, Pontificia Universidad Católica de Chile. From 2014 to 2016, he was a Research Associate with the Control and Power Group in the Electrical and Electronic Engineering Department at Imperial College London, London, U.K. He is also a Research Associate with the Solar Energy Research Center (SERC Chile) and the Universidad Católica (UC) Energy Research Center, both in Santiago. He is the Principal Investigator of the Electric Vehicle Laboratory and the Power and Energy Conversion Laboratory (PEClab) with the Pontificia Universidad Católica de Chile. His research interests are power electronics and control applied to electric vehicles, ac and dc electric networks, microgrids, renewable energy, industrial applications, and motor drives.

Jon Clare (M'90–SM'04) was born in Bristol, U.K., in 1957. He received the B.Sc. and Ph.D. degrees in electrical engineering from the University of Bristol, Bristol, U.K., in 1979 and 1983, respectively.

From 1984 to 1990, he was a Research Assistant and Lecturer with the University of Bristol, where he was involved in teaching and research on power electronic systems. Since 1990, he has been with the Power Electronics, Machines and Control Group, University of Nottingham, Nottingham, U.K., where he is currently a Professor of Power Electronics. His research interests include power-electronic converters and modulation strategies, variable-speed-drive systems, and electromagnetic compatibility.

Ralph Kennel (M'90–SM'96) received the Diploma and the Dr.-Ing. (Ph.D.) degrees in electrical engineering from the University of Kaiserslautern, Kaiserslautern, Germany, in 1979 and 1984, respectively.

From 1983 to 1999, he was with Robert BOSCH GmbH, Stuttgart, Germany, working in several roles; until 1997, he was responsible for the development of servo drives. From 1994 to 1999, he was appointed as a Visiting Professor with the University of Newcastle upon Tyne, Newcastle upon Tyne, U.K. From 1999 to 2008, he was a Professor of Electrical Machines and Drives with Wuppertal University, Wuppertal, Germany. Since 2008, he has been a Professor of Electrical Drive Systems and Power Electronics with Technische Universtat Muenchen, Munich, Germany. His main research interests include sensorless control of ac drives, predictive control of power electronics, and hardware-in-the-loop systems.